Research Project Report

Linear Dynamics of an Elastic Missile

Omri Bar Zeev

Advisors: D. Raveh and M. Idan

July 13, 2025

Abstract

This research project deals with constructing and analyzing the linear dynamics and aerodynamics of an elastic missile. The aeroelastic model was obtained using the RFA method in the commercial software ZAERO, and was then transformed into a linear state-space model. The modes of this model were analyzed by classifying their poles in the complex plane and using Bode plots. V-G plots were then used to understand the aeroelastic coupling of the system. For control and future research purposes, the model was expanded to include moving fins, inertial (IMU) and strain sensors' output, and the Dryden wind model. Numerical simulation of the model was then conducted to support and verify the analytical results, focusing mainly on the short-period dynamics of the missile. These results and simulations will be central to future research efforts focused on controller design for flexible missiles while better accounting for the interactions between the various sensors in the system.

Contents

1 Introduction

As modern missiles increasingly incorporate lightweight and flexible materials, the interaction between structural dynamics and flight mechanics becomes more significant. Unlike traditional rigid-body models, the aeroelastic behavior of these flexible structures introduces complex dynamic phenomena, such as flutter, gust response, and control-induced instabilities. Accurately modeling these interactions is crucial for predicting flight performance, stability, and control behavior under various operating conditions.

Following the approach described by Baldelli et al. (2006), this project develops a linear aeroelastic model to describe the dynamics of a missile in supersonic flight. A finite element model is first constructed to establish the missile's structural properties, and calculate its elastic modes. Based on this model, the aeroelastic forces are calculated using the Doublet Lattice Method (DLM) in ZAERO. Since the aerodynamic forces are initially computed in the frequency domain, they are transformed into the time domain using Rational Function Approximation (RFA), following the minimum state method introduced by Karpel (1980). This transformation enables the construction of a state-space representation, incorporating the missiles actuators and sensors, such as IMU and optical strain sensors, enabling improved control performance compared to traditional rigid-body models that use only IMU, relating their reading to body states only.

To validate the model, classical analysis techniques are employed, including eigenvalue map, Bode plots, and $\omega - V - g$ plot. Additionally, system response simulations are conducted to verify the conclusions drawn from the model analysis and to assess the model's capability to accurately simulate the missile's dynamic behavior under various inputs.

2 Mathematical Model

This section presents the formulation of a linear aeroelastic model suitable for control design and state estimation using a Kalman filter. The governing equations of motion are derived using a modal representation, significantly reducing the computational burden while preserving the dominant structural dynamics. The aerodynamic forces, originally computed in the frequency domain, are transformed into a rational function approximation (RFA) to facilitate their integration into a state-space representation. Using the state-space representation, actuators and sensors, such as IMU and fiber optic strain sensors are, introduced in the model. The resulting aeroelastic state-space model provides a framework for implementing advanced control and estimation techniques, incorporating structural damping, control surface inputs, and atmospheric gust disturbances.

2.1 Aeroelastic Model

The basic equations of motions, that describe an aeroelastic system, containing inertial, stiffness and unsteady aerodynamic forces are

$$[M]\{\ddot{q}\} + \left([K] - \rho V^2 [A(ik)]\right)\{q\} = \{0\}, \tag{1}$$

where q is the physical coordinates vector of the problem, $[M]$ is the mass matrix, $[K]$ is the stiffness matrix and $[A(ik)]$ is the aerodynamic influence coefficients matrix. k is the reduced frequency defined as $k = \omega L/V$, where V is the airspeed, ω is the frequency and L is a characteristic length. The aerodynamic force vector is a nonlinear function of the airspeed. Hence, a different ASE state-space model can be obtained for each airspeed by fixing the airspeed value. Additionally, the dimension of these EOMs is very high, since typical finite-element models include thousands of DOFs at best. To reduce dimensionality, the EOM is transformed to modal coordinates

$$\{q\} = [\phi]\{\xi\}, \tag{2}$$

where the displacements at the physical coordinates are represented as a combination of a set of structural modes, incorporated in the structural modes matrix $[\phi]$, with their modal participation coefficients $\{\xi\}$ (also referred to as modal displacements). In this manner, the missile can be modeled using only the dominant structural modes, thus achieving significant order reduction. By applying (2) to (1), the aeroelastic EOM expressed in modal coordinates are expressed as

$$\overbrace{[\phi]^T [M] [\phi]}^{M_{hh}} \left\{\ddot{\xi}\right\} + \overbrace{[\phi]^T [K] [\phi]}^{K_{hh}} \{\xi\} = \rho V^2 \overbrace{[\phi]^T [A(ik)] [\phi]}^{[Q(ik)]} \{\xi\}, \tag{3}$$

where the matrices $[M_{hh}]$ and $[K_{hh}]$ are the generalized mass and stiffness matrices, respectively, and $[Q\,(ik)]$ is the aerodynamic influence coefficient matrix, written in modal coordinates. Introducing structural damping, control surfaces and atmospheric gust input, (3) can take a more general form

$$[M_{hh}]\{\ddot{\xi}\} + [C_{hh}]\{\dot{\xi}\} + [K_{hh}]\{\xi\} + [M_{hc}]\{\ddot{\delta}\} = \\ = q_\infty [Q_{hh}(ik)]\{\xi\} + q_\infty [Q_{hc}(ik)]\{\delta\} + q_\infty \{Q_{hg}(ik)\}(w_G/V), \quad (4)$$

where δ is the control surface deflection vector, w_G/V is the vertical gust velocity, w_G, normalized by airspeed, and q_∞ is the dynamic pressure. The matrix $[C_{hh}]$ is the generalized damping and $[M_{hc}]$ is the generalized control coupling mass matrices, respectively. The subscript h and c relate to the natural structural modes and the control surfaces, respectively. $[Q_{hh}(ik)]$ and $[Q_{hc}(ik)]$ are the Generalized Aerodynamic Force (GAF) matrices due to structural modes and control surface kinematic modes, respectively, and $\{Q_{hg}(ik)\}$ is the gust column.

2.2 Rational Function Approximation

One of the major issues in the formulation of the state-space EOM for an aeroelastic system is that the GAF matrices are computed in the frequency domain. They must be converted to a rational function form to be incorporated in the state-space equations. The technique used to convert the GAF matrices is the Rational Function Approximation (RFA), which transforms each element of the GAF matrices to a rational function in the entire complex domain, using the complex Laplace variable s, based on frequency-dependent tabulated data. The form of the RFA used to convert the GAF matrices is

$$[\tilde{Q}(s)] = [Q_{hh}(s), Q_{hc}(s), Q_{hg}(s)] = [A_{hh_0}, A_{hc_0}, A_{hg_0}] + \frac{L}{V}[A_{hh_1}, A_{hc_1}, A_{hg_1}]\,s + \\ + \frac{L^2}{V^2}[A_{hh_2}, A_{hc_2}, A_{hg_2}]\,s^2 + [D]\left[s[I] - \frac{V}{L}[R]\right]^{-1}[E_h, E_c, E_g]\,s, \quad (5)$$

where $[A_{hg_2}]$ is set to zero to avoid coefficients related to the second time derivative of the gust velocity. The augmenting aerodynamic state vector is then defined as

$$\{x_a\} = \left[s[I] - \frac{V}{L}[R]\right]^{-1}[[E_h]\{\xi\} + [E_c]\{\delta\} + [E_g]\{\bar{w}_g\}]\,s, \quad (6)$$

where

$$\bar{w}_g = \left\{ \begin{array}{c} \frac{w_g}{V} \\ \frac{\dot{w}_g}{V} \end{array} \right\}. \quad (7)$$

2.3 Aeroelastic State Space Equations

To get the state-space EOM for the aeroelastic model, define the aeroelastic state vector as

$$x_{ae} = \left\{ \begin{array}{c} \xi \\ \dot{\xi} \\ x_a \end{array} \right\}. \tag{8}$$

Substituting (5) and (6) into (4), the aeroelastic state-space equations are expressed as

$$\{\dot{x}_{ae}\} = [A_{ae}]\{x_{ae}\} + [B_{ae}]\{u_{ae}\} + [B_{aw}]\{\bar{w}_g\}, \tag{9}$$

$$\{y_{ae}\} = [C_{ae}]\{x_{ae}\} + [D_{ae}]\{u_{ae}\} + [C_{aw}]\{\bar{w}_g\}, \tag{10}$$

where

$$\{u_{ae}\} = \{\delta, \dot{\delta}, \ddot{\delta}\}, \tag{11}$$

$$[\bar{M}] = \left[[M_{hh}] - \frac{q_\infty L^2}{V^2}[A_{hh_2}]\right], \tag{12}$$

$$[A_{ae}] = \begin{bmatrix} [0] & [I] & [0] \\ -[\bar{M}]^{-1}\left[[K_{hh}] - q_\infty [A_{hh_0}]\right] & -[\bar{M}]^{-1}\left[[C_{hh}] - q_\infty \frac{L}{V}[A_{hh_1}]\right] & q_\infty [\bar{M}]^{-1}[D] \\ [0] & [E_h] & \frac{V}{L}[R] \end{bmatrix}, \tag{13}$$

$$[B_{ae}] = \begin{bmatrix} [0] & [0] & [0] \\ q_\infty [\bar{M}]^{-1}[A_{hc_0}] & q_\infty \frac{L}{V}[\bar{M}]^{-1}[A_{hc_1}] & -[\bar{M}]^{-1}\left[[M_{hc}] - \frac{q_\infty L^2}{V^2}[A_{hc_2}]\right] \\ [0] & [E_c] & [0] \end{bmatrix}, \tag{14}$$

$$[B_{aw}] = \begin{bmatrix} [0] & [0] \\ q_\infty [\bar{M}]^{-1}[A_{hg_0}] & q_\infty \frac{L}{V}[\bar{M}]^{-1}[A_{hg_1}] \\ [0] & [E_g] \end{bmatrix}. \tag{15}$$

The form of $[C_{ae}], [D_{ae}], [C_{aw}]$ is sensor-dependent. For example, for an acceleration sensor, (10) is

$$
\begin{aligned}
&y_{ae_i} = \\
&-\phi_{h_i}[\bar{M}]^{-1}\left[[[K_{hh}]-q_\infty[A_{hh_0}]], \left[[C_{hh}]-q_\infty\frac{L}{V}[A_{hh_1}]\right], q_\infty[D]\right]\{X_{ae}\} \\
&-\phi_{h_i}[\bar{M}]^{-1}\left[q_\infty[A_{hc_0}], q_\infty\frac{L}{V}[A_{hc_1}], \left[[M_{hc}]-\frac{q_\infty L^2}{V^2}[A_{hc_2}]\right]\right]\{U_{ae}\} \\
&-\phi_{h_i}[\bar{M}]^{-1}\left[q_\infty[A_{hg_0}], q_\infty\frac{L}{V}[A_{hg_1}]\right]\{\bar{w}_g\},
\end{aligned}
\tag{16}
$$

where ϕ_{h_i} is the modal displacements of the modes at the sensor location. Focusing on two main types of measurements, stain measurements and IMU measurements (acceleration and angular rates), denoted accordingly by $(\ )_{st}$ and $(\ )_{IMU}$, the measurements are

$$
\{y_{st}\} = [\Psi_s]\{\xi\} = \begin{bmatrix}[\Psi_s] & 0 & 0\end{bmatrix}\{x_{ae}\} + v_k^{st}, \tag{17}
$$

$$
\begin{aligned}
&\{y_{IMU}\} = \begin{Bmatrix} a_{meas} \\ \dot{\theta}_{meas}\end{Bmatrix} = \begin{Bmatrix}[\Phi]\ddot{\xi} \\ [\Phi_r]\dot{\xi}\end{Bmatrix} \\
&= \begin{bmatrix} -[\Phi][\bar{M}]^{-1}[[K_{hh}]-q_\infty[A_{hh_0}]] & -[\Phi][\bar{M}]^{-1}\left[[C_{hh}]-q_\infty\frac{L}{V}[A_{hh_1}]\right] & -q_\infty[\Phi][\bar{M}]^{-1}[D] \\ [0] & [\Phi_r] & [0]\end{bmatrix}\{x_{ae}\} \\
&+ \begin{bmatrix} -q_\infty[\Phi][\bar{M}]^{-1}[A_{hc_0}] & -q_\infty\frac{L}{V}[\Phi][\bar{M}]^{-1}[A_{hc_1}] & -[\Phi][\bar{M}]^{-1}\left[[M_{hc}]-\frac{q_\infty L^2}{V^2}[A_{hc_2}]\right] \\ [0] & [0] & [0]\end{bmatrix}\{u_{ae}\} \\
&+ \begin{bmatrix} -q_\infty[\Phi][\bar{M}]^{-1}[A_{hg_0}] & -q_\infty\frac{L}{V}[\Phi][\bar{M}]^{-1}[A_{hg_1}] \\ [0] & [0]\end{bmatrix}\{\bar{w}_g\} + v_k^{IMU},
\end{aligned}
\tag{18}
$$

where $[\Psi_s]$ is the matrix of the strain modes of the model.

3 Test Case

To evaluate the structural and aerodynamic characteristics of the missile, a comprehensive test case is developed, combining finite element modeling and aerodynamic analysis. This section details the construction of the finite element (FE) model in MSC NASTRAN, the extraction of modal properties, and the generation of an aerodynamic model using ZAERO.

3.1 Finite Element Model

A finite element model is generated in MSC NASTRAN, based on the model used by Genkin and Raveh (2024). The tested modeled is a 6 meter long missile, made out of shell elements, connected by rigid-body elements (RBE) to a beam element in the center of the missile. Also, a concentrated mass element was added, in order for the model to be more realistic and take the center of mass forward. Four fins were added in an X configuration to the model. The fins were attached to the shell elements using RBEs. The RBEs were connected to 3 nodes in the fin and body shell. The generated model is depicted in Fig. 1

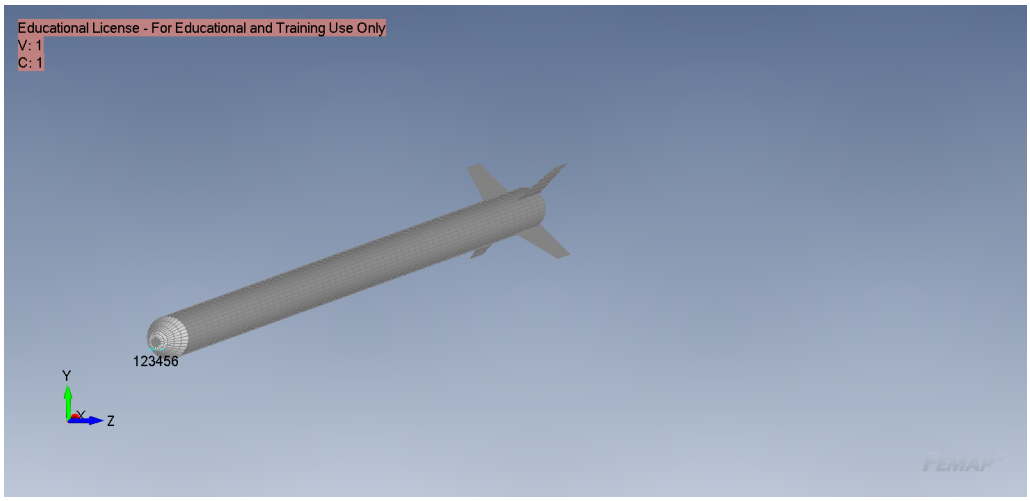

Figure 1: FE model of the missile

Using the FE model, a normal modes analysis was performed. In the analysis, 20 modes were calculated. The analysis was performed using two different solvers: one using `EIGRL` which solves the equation using the Lanczos solver, and another using `EIGR` using the Givens method. The differences will be discussed later in the project.

The first six modes are rigid-body modes. Using the Lanczos solver, these modes are computed about the principle axes. I.e., they are not purely displacement/rotation about the global coordinate system axes, but rather involve coupled displacements. Using the Givens solver produces pure modes, involving X,Y,Z

Table 1: Calculated Normal modes - frequencies and types

Mode Number	Frequency [Hz]	Mode type
1-6	0	Rigid body
7-8	11.9	First bending
9-10	33.05	Second bending
11-12	65.87	Third bending
13-14	104.51	Forth bending
16	120.23	First torsion
17-18	130.38	Fifth bending
19	148.67	Compression mode

direction displacement/rotation about the aircraft center of gravity. It is also important to note that the Lanczos solver solution is much faster and as such it was mainly used.

The modes are presented in Table 1. All bending modes appear in pairs, meaning each bending frequency is associated with two modes. This occurs because the model is three-dimensional, allowing the aircraft to bend in both principal directions perpendicular to the X-axis. These pairs of modes share the same physical properties but are oriented 90 degrees apart (in rotation around X axis). Modes 15 and 20 were omitted in Table 1, as they correspond to fin motions that are not physically accurate in the current model and will be properly defined later in ZAERO during control surface setup. Since the primary focus of this work is on modeling the overall dynamics of a missile for control system purposes, only the first 12 modes are considered. Modes with frequencies above 100 Hz are expected to have a negligible impact on the system's dynamic response. The first six elastic modes are depicted in Fig. 2.

In addition, the corresponding strain modes of the system are needed for the analysis and sensor simulation, in order to be able to create a measurement according to (17). As such, the NASTRAN command `STRAIN`, which outputs the corresponding strain of the modes for a given set, was used. As the simulated sensor is a Fiber-optic strain sensor, which measures the principle strain in the X direction (stretch-compression) in specific points, a set of points along a straight line was chosen, highlighted in the model in Fig. 3.

All of the results, particularly the strain results, need to be extracted from the output file. The extraction is performed into a `.h5` file (using `MDLPRM HDF5 0`), a file that can be read easily by a dedicated MATLAB function. As with any FE software, the data is computed at the nodes. To determine the strain value at the center of each element, which is where the desired sensor spot is, the strain values at the element's nodes are located and averaged to approximate the strain at the midpoint. The data is then organized into a matrix with 13 rows (one for each

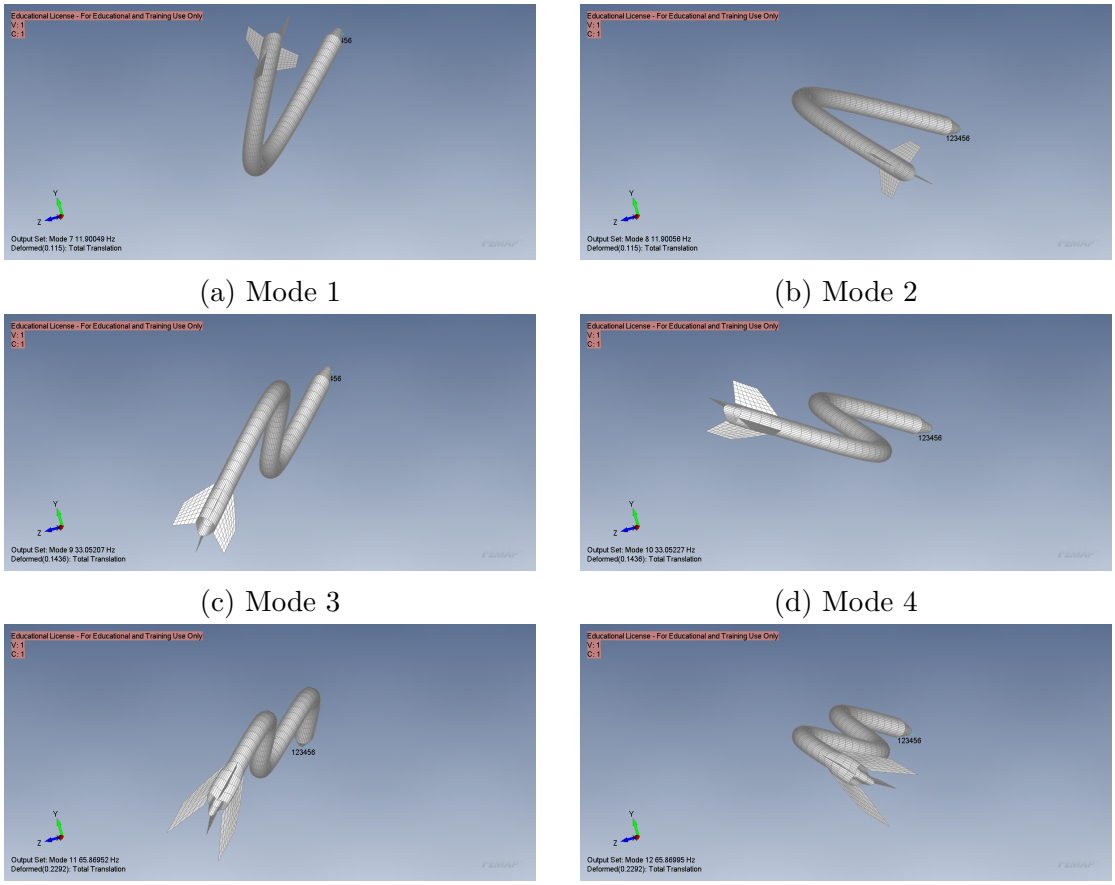

(a) Mode 1 (b) Mode 2

(c) Mode 3 (d) Mode 4

(e) Mode 5 (f) Mode 6

Figure 2: The first six elastic modes of the system.

element-sensor) and 12 columns (one for each mode used). Finally, the sampled strain modes can be visualized by plotting the columns of the strain matrix with respect to position along the missile, as shown in Fig. 4.

As expected, the first six modes have numerically zero amplitude, reflecting their association with rigid-body motion, which does not produce strain. The subsequent six modes correspond to the first six elastic modes, consisting of three pairs of bending modes. These show low amplitude near the tips, where deflections are largest, which aligns with the strain distribution of a cantilever beam. This consistency indicates that the calculated strain modes are physically accurate. Additionally, the mode shapes are well captured, suggesting that the number and placement of measurement points are sufficient for accurately representing these modes.

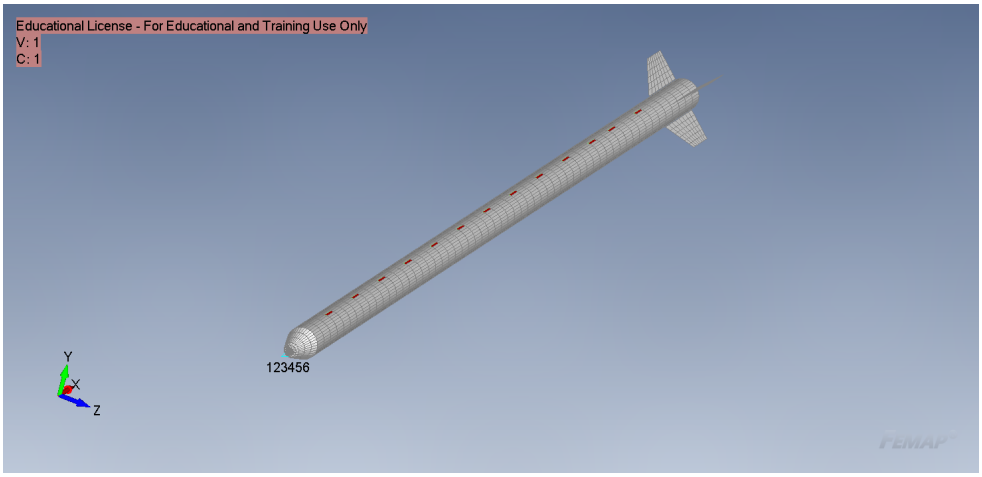

Figure 3: FE model of the missile – elements for which the strain was extracted are highlighted

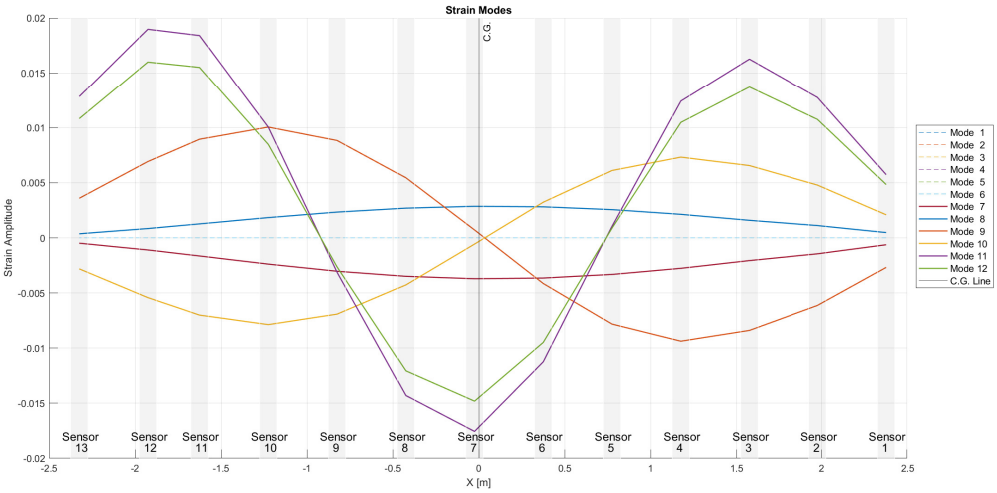

Figure 4: 12 First strain modes

3.2 Panel Model and ZAERO Code

The aerodynamic model is obtained by ZAERO, a commercial panel method programs that uses DLM to solve for the missile aerodynamics coefficients and matrices. This subsection will explain the code and parameters of the ZAERO program.

First, the problem dimensions and reference values are defined. The reference length is taken as the missile length, $L = 6[m]$, and the reference area is defined as the cross-sectional area, $A = 2\pi Rt$, where t represents the shell thickness of the cross-section.

Doublet panels are then placed to represent the missile aerodynamics. They are places over the shell elements of the finite element model, using the `SEGMESH` and `BODY7` cards. Spline, which connects all of the structural and aerodynamic nodes, is performed and the interpolated modes are extracted in order to verify the

results up to this point with the results from MSC NASTRAN that were presented earlier.

After that, the control surfaces are generated. The aerodynamic panels are being generated and distributed over the control surface using `CAERO7`, implementing the NACA-0012 airfoil properties. A greater number of nodes for the aerodynamic model of the fin than the structural one is needed, in order to match the true airfoil aerodynamics. The control surfaces are attached to the single connecting point in the FE model and are then defined as an aerodynamic control surface. In that process, the axis of rotation is defined for the aerodynamic surface. Finally, the aerodynamic surfaces modes can be extracted and inspected. An example of such mode is shown in Fig. 5.

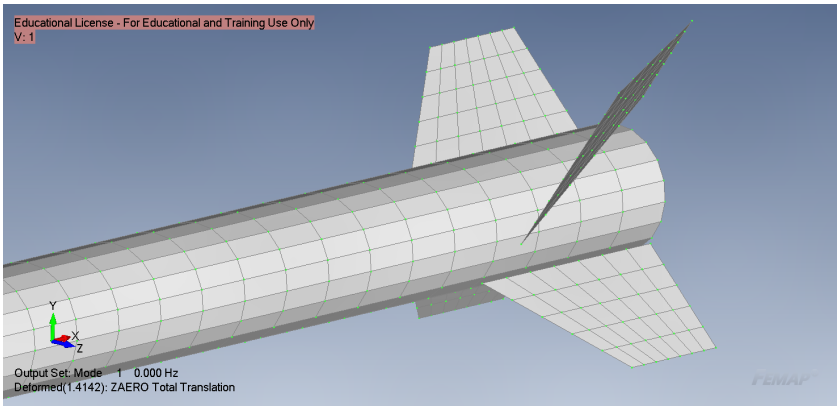

Figure 5: Control Surface mode

An actuator transfer function must be defined within the program. For simplicity, a third-order transfer function is selected, with parameters chosen such that its poles are placed far from the system's other poles. This ensures minimal interaction between the control surfaces and the overall system dynamics. The selected transfer function is

$$\begin{aligned} &\frac{\delta}{u_{ac}} = \frac{A_0}{s^3 + A_2 s^2 + A_1 s + A_0}, \\ &A_0 = 27\omega_{max}^3, \quad A_1 = 13.5\omega_{max}^2, \quad A_2 = 4.5\omega_{max}^3, \end{aligned} \tag{19}$$

where ω_{max} is the largest normal mode frequency used in the analysis.

With that, the aerodynamic modeling is completed, and the ZAERO analysis is performed to obtain all the necessary matrices for the model presented in subsection section 2.3. The generated model will be tested in two subcases. In the first subcase, a gust analysis is performed to extract all the matrices described in section 2.3. In the second subcase, a flutter analysis is performed to validate certain results obtained in the first case.

In the first subcase, the aerodynamic properties are first defined using the

MKAEROZ card. The flight Mach number is set to $M = 2$, and a list of all non-dimensional frequencies k to be used in the calculations is specified. Next, the gust properties are defined using the GENGUST card, followed by the main analysis card, GLOADS. Within the GLOADS card, the system is defined along with the control system inputs and outputs specified in the ASECONT card. A reference is also made to the MINSTAT card, which calculates the RFA matrices according to section 2.2. Additionally, the MLDSTAT card is referenced to define the states used in the analysis, following Baldelli et al. (2006). The chosen states are

$$x_{rigid} = \left\{ X, Y, H, \Phi, \Theta, \Psi, U, V, W, P, Q, R \right\}^T. \tag{20}$$

By choosing to work with these states, any rigid mode calculated by the NASTRAN program are essentially ignored, as it does not represent a "pure" rigid body modes. Furthermore, it is also possible to include the angle of attack α, the slip angle β in the state vector, instead of W, V respectively, to describe the full aircraft state.

Next, the control system is defined. The input of the system, previously defined as the control surfaces, is now complemented by the output of the system. To simulate an IMU, three perpendicular accelerometers and gyros are needed. The three accelerometers, one in each direction, are placed near the tip of the missile, and direct measurements of P, Q, R are taken, simulating the gyros. Finally, all matrices are exported in OUTPUT4 format using the ASEOUT card, which outputs the control matrices A, B, C, D, or via the MINSTAT card, which exports the RFA matrices A_0, A_1, A_2, D, E.

In the second subcase, a classical flutter analysis is performed using the K-method, a well-known method, thoroughly described by Bisplinghoff et al. (2013). A predefined set of flight velocities is considered, and for each velocity, an eigenvalue problem is solved to determine the system's aeroelastic response. Specifically, the K-method formulates the flutter analysis as a frequency-domain eigenvalue problem, where the reduced frequency is treated as an eigenvalue parameter. From the resulting eigenvalues, the aeroelastic frequencies, damping ratios, and corresponding flutter velocities can be extracted.

The eigenvalue problem that is solved is stated as

$$\begin{aligned} &\left(\underbrace{[M_{hh}] + \rho \frac{b^2}{k^2}[Q_{hh}(ik)]}_{F} - \underbrace{\frac{1 + jg}{\omega^2}}_{\lambda}[K_{hh}] \right) \{u_0\} = \{0\}, \\ &\Rightarrow \omega_i = \sqrt{\frac{1}{\mathrm{Re}\{\lambda_i\}}}, \quad g_i = \frac{\mathrm{Im}\{\lambda_i\}}{\mathrm{Re}\{\lambda_i\}}, \quad V_i = \frac{\omega_i b}{k_i}. \end{aligned} \tag{21}$$

For each velocity, a frequency ω is computed, representing the true oscillation frequency of the system when a fictitious damping g is introduced. This approach captures the effect of unsteady aerodynamic forces, meaning the calculated frequency reflects the actual dynamic behavior of the system at that velocity—distinct from the structural modal frequencies listed in Table 1. The results can be visualized using the `PLOTVG` command.

4 Results

In this section, ZAERO results will be presented and analyzed. Subsequently, a simulation of the system dynamics will be conducted, and the response to specific control surface and gust inputs will be computed.

4.1 ZAERO Results

The following linear dynamics equations for a certain velocity were retrieved using the matrices $A_{ae}, B_{ae}, B_{aw}, C_{ae}, D_{ae}, C_{aw}$, calculated and outputted by ZAERO,

$$\{\dot{x}_{ae}\} = [A_{ae}]\{x_{ae}\} + [B_{ae}]\{u_{ae}\} + [B_{aw}]\{\bar{w}_g\}, \tag{22}$$

$$\{y_{ae}\} = [C_{ae}]\{x_{ae}\} + [D_{ae}]\{u_{ae}\} + [C_{aw}]\{\bar{w}_g\}, \tag{23}$$

where the state vector is made out of the a rigid part as in (20), its derivatives, normal modes participation coefficients and their respective derivatives, the aerodynamic lags of the RFA, according to (6), (8) and (13), and the actuator modes according to the state space realization of the actuator transfer function (19) for each actuator.

One way to examine and verify the results is to analyze the eigenvalues of the dynamics matrix A_{ae} that represent the poles of the aeroelastic system and a future closed-loop system. Classifying the eigenvalues by their respective meaning (e.g. structural modes, actuator modes, etc.), is the first verification step. First, all eigenvalues are presented in the complex plane in Fig. 6.

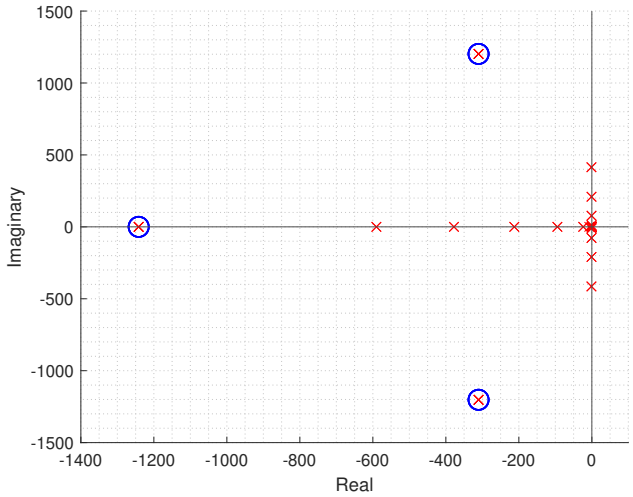

Figure 6: Eigenvalue map

As observed, there is a dense cluster of eigenvalues near the origin, along with a distinct group of three eigenvalues positioned farther away (marked blue). These

marked eigenvalues represent a set of three eigenvalues, repeated four times: one for each actuator dynamic of a third-order model of (19). Since the actuator dynamics were designed to avoid interaction with the system dynamics, their poles were placed far from the origin, ensuring minimal influence. These poles correspond to a frequency of $197Hz$, which translates to a time constant of 0.005 seconds, a very short duration compared to the typical time scale of the system's normal modes.

The eigenvalue map can be further zoomed-in to examine additional eigenvalues in greater detail, as depicted in Fig. 7. In Fig. 7a, a group of five real eigenvalues (doubled) is observed. These correspond to the aerodynamic lags and gust lag roots introduced by the RFA to approximate the tabulated nonlinear effects of Q_{hh} and Q_{hg}. These lags exhibit much faster dynamics compared to the main system (located near the center), but their time scale is comparable to that of the elastic mode eigenvalues, which are highlighted in Fig. 7b. The elastic modes eigenvalues align with expectations, having a frequency similar, though not identical, to the rigid body modes due to aeroelastic interactions between modes, which will be discussed later. Their damping is determined by the RFA formulation.

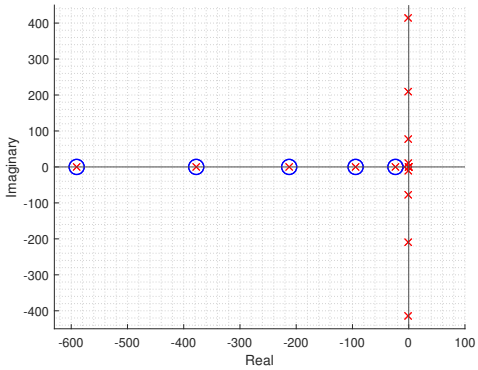

(a) Eigenvalue map – zoom-in 1

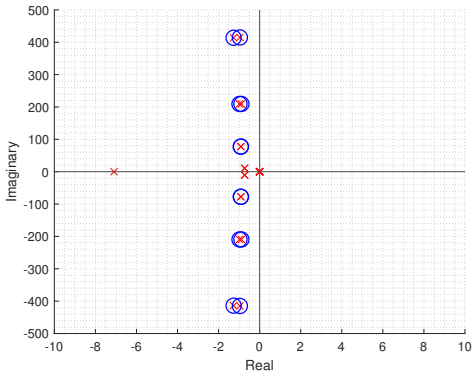

(b) Eigenvalue map – zoom-in 2

Figure 7: Eigenvalue map - zoom-in views

Finally, the rigid body dynamics eigenvalues of the system can be inspected, in Fig. 8. Two (doubled) complex eigenvalues are observed, corresponding to the short-period (SP) dynamics of the system. These eigenvalues appear in pairs due to the 3D nature of the dynamics and the symmetry of the vehicle, which results in identical SP dynamics for both longitudinal and lateral motion. Additionally, a real pole is present with a time constant of approximately 1/7 seconds, which can be associated with the roll dynamics of the system. Lastly, a group of numerically zero poles is identified, representing the integration of various states into position, as well as dynamics not yet specified, such as phugoid motion related to gravity, which was not included in this model and will be added in future work.

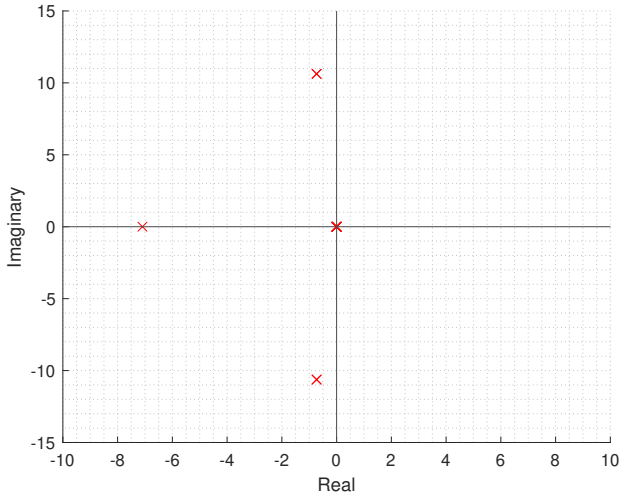

Figure 8: Eigenvalue map – zoom-in 3

For further analysis from a different perspective, the system's Bode plots can be examined in Figs. 9–11. The three Bode plots are of a transfer functions between each actuator input to a different sensor: a Z-direction accelerometer, a pitch rate sensor, and one of the many fiber optic strain sensors (FOSS), all of which are defined in (17) and (18).

Both Figs. 10 and 11 and Figs. 6, 7a, 7b and 8 present the same results from different perspectives. While the Bode plots make it easier to quantify amplitudes and frequencies, the eigenvalue maps offer valuable insight into the system's stability and modal behavior by clearly showing the location and separation of the poles in the complex plane. Note that the main difference in the results is the effect the zeros of each transfer functions have on the corresponding output. As seen in all of the outputs for the different inputs in Fig. 9, the acceleration dynamics are dominated by four main frequencies. Three frequencies are the elastic mode frequencies and are correlated with the results shown previously. There is an extra frequency of $\sim 10[rad/sec]$ which is the short-period frequency. In the

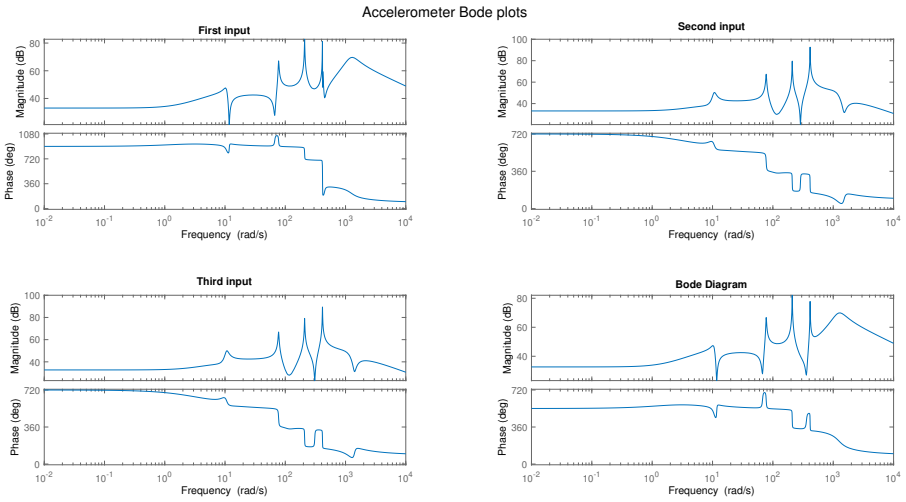

Figure 9: Accelerometer Bode to each input

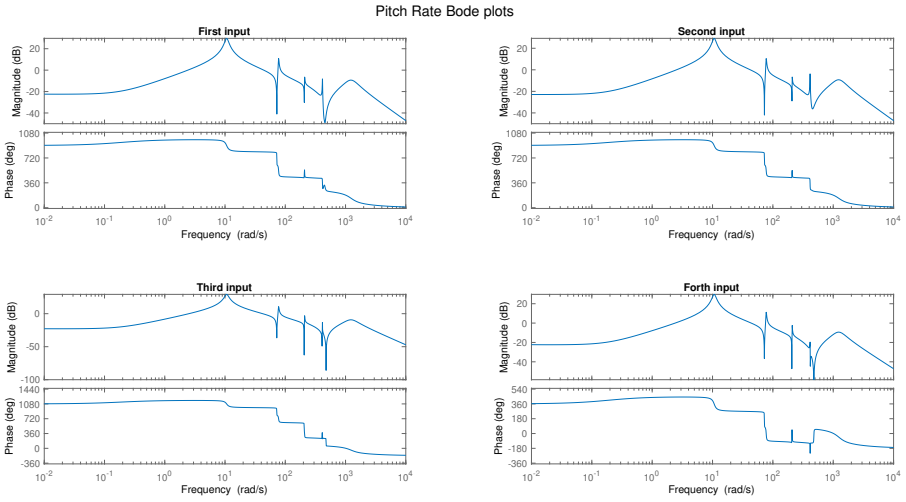

Figure 10: Pitch Rate Bode to each input

Bode plots Figs. 9 and 10, amplification is observed at frequencies higher than those typically associated with flight dynamics. In a purely rigid body model, this amplification would not be present, as it would not capture the high-frequency dynamics introduced by the flexible modes of the system.

In Figs. 9–11, the elastic mode amplitudes are orders of magnitude smaller than the system's rigid-body dynamic amplitude or the zero-frequency response. This shows that none of the sensors will measure a purely rigid-body dynamic response. Instead, all sensors will measure both rigid-body dynamics (e.g., short-period motion) and elastic deformations.

Interestingly, the FOSS sensor, shown in Fig. 11, is affected by the short-period mode, despite being a strain sensor. Since strain is typically unaffected by rigid body motion, this implies that the short-period mode is not purely a rigid-body

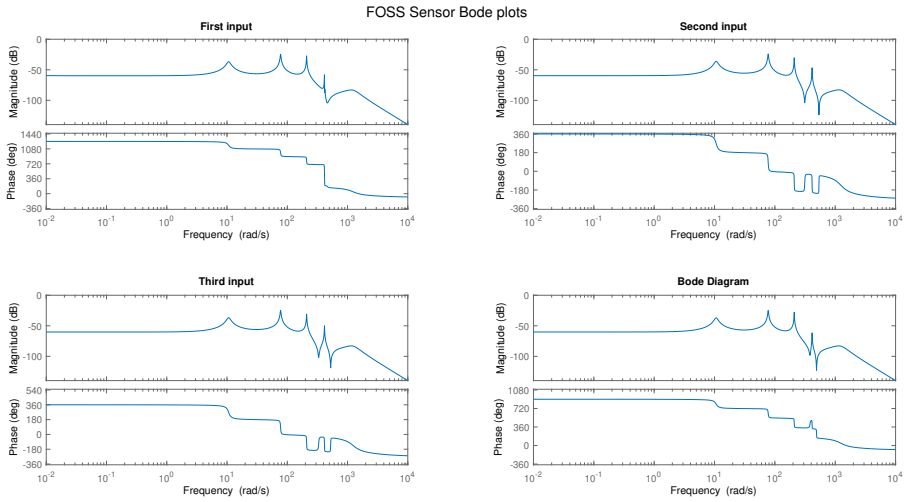

Figure 11: FOSS Bode to each input for sensor number 4 in the sensor array

phenomenon but rather a coupled rigid-elastic interaction. This observation will be further analyzed and confirmed later using an $\omega - V - g$ plot.

Additionally, at frequencies lower than the short-period mode, the response exhibits a relatively constant amplitude. The absence of a distinct peak in this low-frequency range indicates that no additional dynamic mode, such as the phugoid, is present. This result is expected, as gravity and drag forces, which are essential for the phugoid mode to occur, were not included in the model. Without these forces, the energy exchange that characterizes phugoid oscillations cannot take place. As a result, this simplified model differs from a full aircraft model and lacks the peak in the Bode plot typically associated with the phugoid mode.

The final result that supports our previous conclusions is the $\omega - V - g$ plot. This plot provides insight into the exact frequencies of the system, accounting for frequency variations caused by unsteady aerodynamics. The $\omega - V - g$ plots obtained from ZAERO are presented in Figs. 12 and 13.

In Fig. 12, in the the frequency graph, there are three upper horizontal lines. These lines originate at zero velocity with a nonzero frequency, indicating that they correspond to the elastic modes. The fact that these frequencies remain nearly constant as velocity increases suggests that the elastic mode frequencies are largely unaffected by changes in velocity. That fact can indicate that the structure is very stiff, and as such the aerodynamic forces are not great enough to change the missile dynamics with increase in velocity.

A closer view of the low-frequency cluster of plots is presented in Fig. 13. There are four graphs of constant zero frequency, these are the rigid body modes that don't interact with elastic modes. There are another two modes that starts with a zero frequency when the velocity is zero, and their frequency rises with velocity.

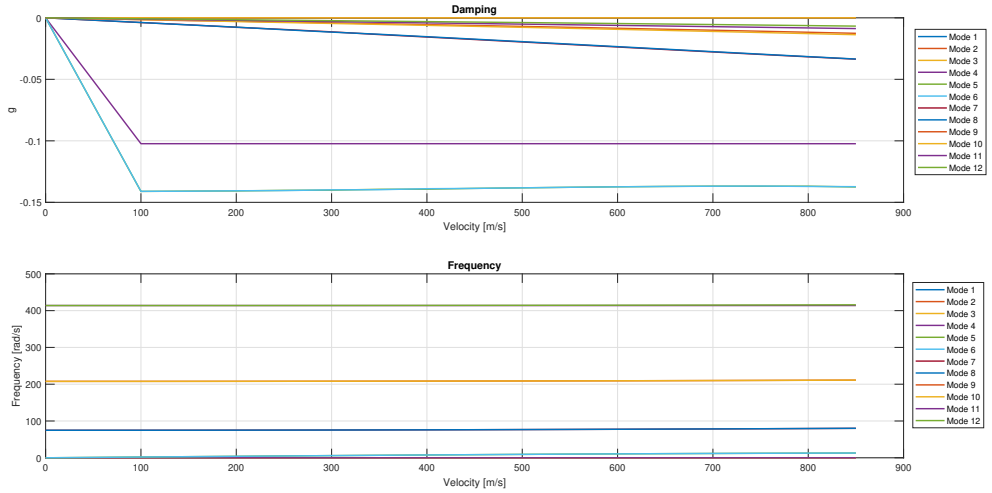

Figure 12: $\omega - V - g$ plot of the aeroelastic system

These modes are an interaction modes between pitch/yaw and an elastic mode. Due to the added aerodynamic stiffness, as seen in the damping (g) graph, the modes becomes a short period mode, with a frequency of 10.628 $[Hz]$, exactly as seen in Figs. 9–11. These results verify the findings using the eigenvalue map and the Bode plots.

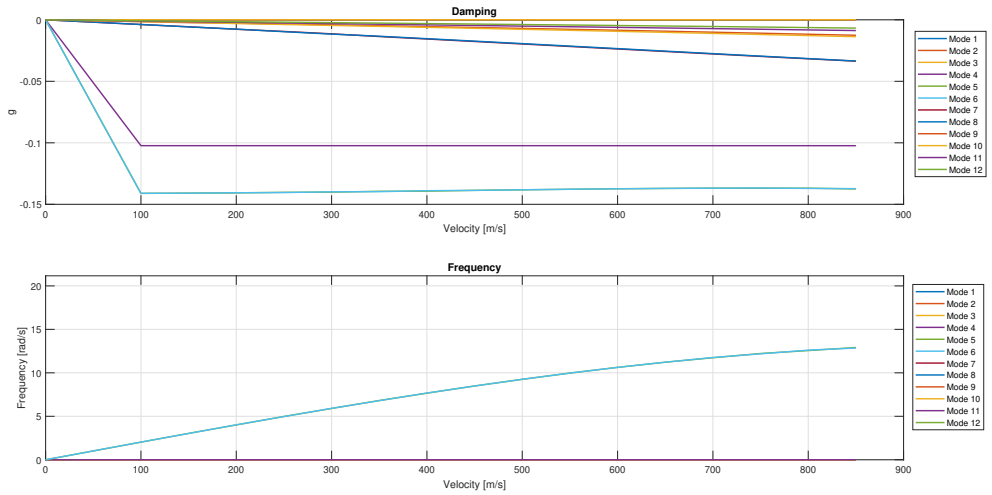

Figure 13: $\omega - V - g$ plot of the aeroelastic system – zoom-in

4.2 Numerical Dynamic Simulation

This subsection prepares the model presented so far for numerical simulations by incorporating stochastic gust and control inputs. It then presents simulation results validating the model.

4.2.1 Implementing the Dryden Wind Model

When modeling stochastic inputs to a system, a wind turbulence model is required. A common choice is Dryden's wind turbulence model, which is designed as a white noise passed through a linear system. The vertical wind model transfer function, as defined by MIL-F-8785C, is given by

$$H_w(s) = \sigma_w \sqrt{\frac{L_w}{\pi V}} \cdot \frac{1 + \frac{\sqrt{3}L_w}{V} s}{\left(1 + \frac{L_w}{V} s\right)^2}, \tag{24}$$

where V represents aircraft's flight speed, and σ_w and L_w are case- and flight condition-dependent parameters.

To incorporate wind input into the system model, its transfer function, H_w, must be expressed in state-space form. Rewriting the transfer function as a standard second-order system with a zero yields

$$\begin{aligned} H_w(s) &= \sigma_w \sqrt{\frac{L_w}{\pi V}} \cdot \frac{1 + \frac{\sqrt{3}L_w}{V} s}{1 + 2\frac{L_w}{V} s + \left(\frac{L_w}{V}\right)^2 s^2} \\ &= \sigma_w \sqrt{\frac{L_w}{\pi V}} \cdot \frac{\frac{\sqrt{3}L_w}{V}\left(s + \frac{1}{\frac{\sqrt{3}L_w}{V}}\right)}{\left(\frac{L_w}{V}\right)^2 \left(s^2 + 2\frac{V}{L_w} s + \left(\frac{V}{L_w}\right)^2\right)}, \end{aligned} \tag{25}$$

$$H_w(s) = \sigma_w \sqrt{\frac{3V}{\pi L_w}} \cdot \frac{s + \frac{V}{\sqrt{3}L_w}}{s^2 + 2\frac{V}{L_w} s + \left(\frac{V}{L_w}\right)^2} = K_w \cdot \frac{s + \beta}{s^2 + 2\zeta\omega_n s + \omega_n^2}. \tag{26}$$

A simulation diagram shown in Fig. 14 is used to generate its state-space representation that will be augmented to the already existing system's state space model. Because of the system's zero, the states will not directly represent the vertical gust and its derivative.

From the simulation diagram, the wind's state space model, derived from a white noise input, can be written as

$$\begin{bmatrix} \dot{x}_1 \\ \dot{x}_2 \end{bmatrix} = \underbrace{\begin{bmatrix} -2\zeta\omega_n & 1 \\ -\omega_n^2 & 0 \end{bmatrix}}_{A_{dry}} \begin{bmatrix} x_1 \\ x_2 \end{bmatrix} + \underbrace{\begin{bmatrix} K_w \\ K_w\beta \end{bmatrix}}_{B_{dry}} u_w \tag{27}$$

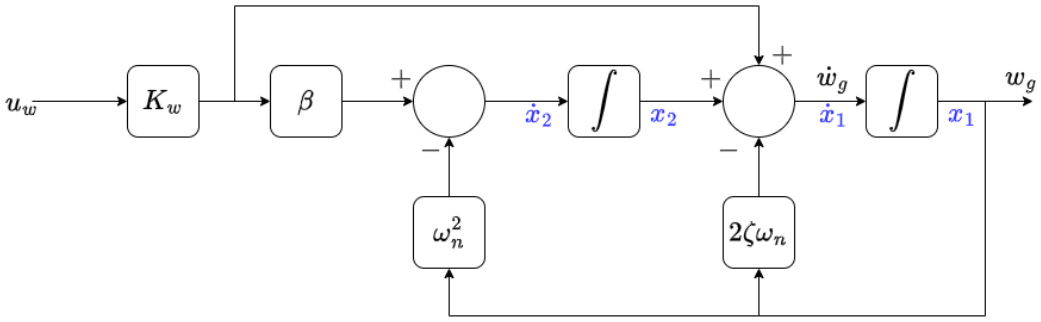

Figure 14: Simulation diagram for the system

with the wind states being

$$\begin{aligned} w_g &= x_1 \\ \dot{w}_g &= K_w u + x_2 - 2\zeta\omega_n x_1 \end{aligned} \Rightarrow \begin{bmatrix} w_g \\ \dot{w}_g \end{bmatrix} = \underbrace{\begin{bmatrix} 1 & 0 \\ -2\zeta\omega_n & 1 \end{bmatrix}}_{A_w} \underbrace{\begin{bmatrix} x_1 \\ x_2 \end{bmatrix}}_{x_w} + \underbrace{\begin{bmatrix} 0 \\ K_w \end{bmatrix}}_{B_w} u_w. \tag{28}$$

It can be seen that in this formulation, the wind derivative output depends on the driving input noise u_w. To avoid thiss undesired effect and assist in the discrete-time formulation, a low-pass filter with a high bandwidth is added to (26) to yield

$$H_w(s) = \sigma_w \sqrt{\frac{3V}{\pi L_w}} \cdot \frac{s + \frac{V}{\sqrt{3}L_w}}{s^2 + 2\frac{V}{L_w}s + \left(\frac{V}{L_w}\right)^2} \frac{\frac{1}{\tau}}{s + \frac{1}{\tau}}, \tag{29}$$

where the filter's time constant is τ. Figure 15 presents a new simulation diagram constructed to develop the corresponding state-space representation. The state-space model of (29) is

$$\begin{bmatrix} \dot{x}_1 \\ \dot{x}_2 \\ \dot{x}_3 \end{bmatrix} = \underbrace{\begin{bmatrix} -\left(2\zeta\omega_n + \frac{1}{\tau}\right) & 1 & 0 \\ -\left(\frac{2\zeta\omega_n}{\tau} + \omega_n^2\right) & 0 & 1 \\ -\frac{\omega_n^2}{\tau} & 0 & 0 \end{bmatrix}}_{A_{dry}} \underbrace{\begin{bmatrix} x_1 \\ x_2 \\ x_3 \end{bmatrix}}_{x_w} + \underbrace{\begin{bmatrix} 0 \\ K_w \\ K_w\beta \end{bmatrix}}_{B_{dry}} u_w, \tag{30}$$

with the new wind states

$$\begin{aligned} w_g &= x_1 \\ \dot{w}_g &= x_2 - (2\zeta\omega_n + \tfrac{1}{\tau})x_1 \end{aligned} \Rightarrow \begin{bmatrix} w_g \\ \dot{w}_g \end{bmatrix} = \underbrace{\begin{bmatrix} 1 & 0 & 0 \\ -\left(2\zeta\omega_n + \frac{1}{\tau}\right) & 1 & 0 \end{bmatrix}}_{C_{dry}} \underbrace{\begin{bmatrix} x_1 \\ x_2 \\ x_3 \end{bmatrix}}_{x_w}, \tag{31}$$

In this formulation, the wind derivative output is not directly dependent on u_w. For practical implementation, A_w is multiplied by $1/V$ (i.e., $A_w = \frac{1}{V}A_w$) since it's always used to calculate $\bar{w}_g$, as defined in (7).

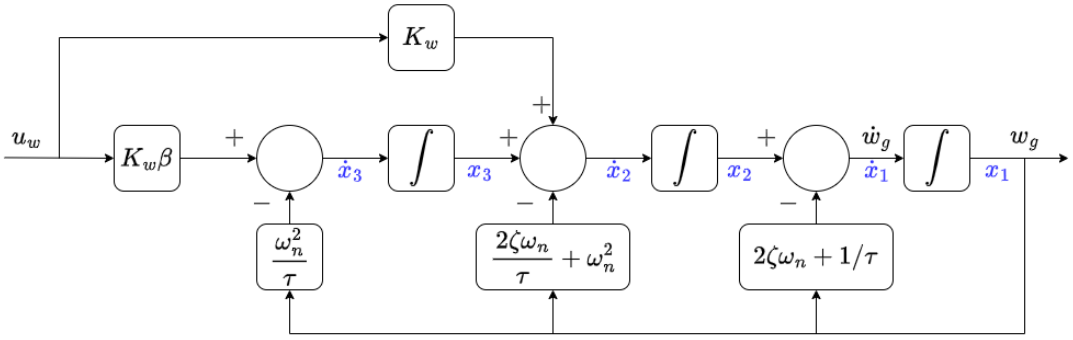

Figure 15: Simulation diagram for the system- with added LPF

The Dryden state-space model can now be incorporated into the aircraft's state-space model derived in section 3 using the expanded state vector

$$x_{ae_{aug}} = \begin{Bmatrix} \xi \\ \dot{\xi} \\ x_a \\ x_w \end{Bmatrix}, \tag{32}$$

where x_w is the added wind state vector. This yields the full augmented state-space equation (based on the expended (22), (30) and (31))

$$\{\dot{x}_{ae}\} = [A_{ae}]\{x_{ae}\} + [B_{ae}]\{u_{ae}\} + [B_{aw}][A_w]\{x_w\}, \tag{33}$$

$$\{\dot{x}_w\} = [A_{dry}]\{x_w\} + [B_{dry}]u_w. \tag{34}$$

Combining (33) and (34), the new state space for $x_{ae_{aug}}$ is

$$\{\dot{x}_{ae_{aug}}\} = \begin{bmatrix} [A_{ae}] & [B_{aw}][A_w] \\ [0] & [A_{dry}] \end{bmatrix} \{x_{ae_{aug}}\} + \begin{bmatrix} [B_{ae}] \\ [0] \end{bmatrix} \{u_{ae}\} + \begin{bmatrix} [0] \\ [B_{dry}] \end{bmatrix} u_w. \tag{35}$$

The measurement equations in (17) and (18) can be augmented similarly, yielding

$$\{y^{st}\} = [C_{ae}^{st}]\{x_{ae}\} + v_k^{st} \tag{36}$$

$$\{y^{IMU}\} = [C_{ae}^{IMU}]\{x_{ae}\} + [D_{ae}^{IMU}]\{u_{ae}\} + [C_{aw}^{IMU}][C_{dry}]\{x_w\} + v_k^{IMU}. \tag{37}$$

These can be transformed into a matrix form for the measurement vector $\begin{Bmatrix} y^{st} \\ y^{IMU} \end{Bmatrix}$ and using the state $\{x_{ae_{aug}}\}$, the measurement model is expressed as

$$\{y_{ae}\} = \begin{bmatrix} C_{ae}^{st} & 0 \\ C_{ae}^{IMU} & C_{aw}^{IMU} A_w \end{bmatrix} \{x_{ae_{aug}}\} + \begin{bmatrix} 0 \\ D_{ae}^{IMU} \end{bmatrix} \{u_{ae}\} + v_k. \tag{38}$$

The system's state-space model presented in (35) and (36) is restated as

$$\{\dot{x}_{ae_{aug}}\} = [\mathcal{A}_{ae}]\{x_{ae_{aug}}\} + [\mathcal{B}_{ae}]\{u_{ae}\} + [\mathcal{B}_{aw}]\{u_w\}, \tag{39}$$

$$\{y_{ae}\} = [\mathcal{C}_{ae}]\{x_{ae_{aug}}\} + [\mathcal{D}_{ae}]\{u_{ae}\} + \{v_k\}, \tag{40}$$

where, $\{v_k\} \sim \mathcal{N}(0, R)$ and $u_w \sim \mathcal{N}(0, 1)$, assuming no correlation between wind and measurement noise $E[vu] = 0$.

4.2.2 Parameter Selection

According to MIL-F-8785C (1980), the typical gust length is $L_w = 1750[ft]$ for medium-high altitudes (above $2000[ft]$). The intensity parameter σ_w is chosen according to Fig. 16. The measurement covariance matrix will be determined using values typical of commercial sensors, as in Genkin and Raveh (2024). Strain measurements are obtained using FOSS with a typical variance of $\sigma_\varepsilon^2 = 5 \cdot 10^{-6}$. The IMU exhibits typical acceleration and angular velocity variances of $\sigma_a^2 = 1 \cdot 10^{-3}$ $[(m/sec^2)^2]$ and $\sigma_{\dot{\theta}}^2 = 5 \cdot 10^{-4}$ $[(rad/sec)^2]$, respectively. These values are then used to construct the measurement covariance matrix

$$R = \begin{bmatrix} \sigma_\varepsilon^2[I]_{N_\varepsilon} & 0 & 0 \\ 0 & \sigma_a^2[I]_{N_a} & 0 \\ 0 & 0 & \sigma_{\dot{\theta}}^2[I]_{N_{\dot{\theta}}} \end{bmatrix} \tag{41}$$

assuming that the measurement noises are independent random variables with Gaussian distribution.

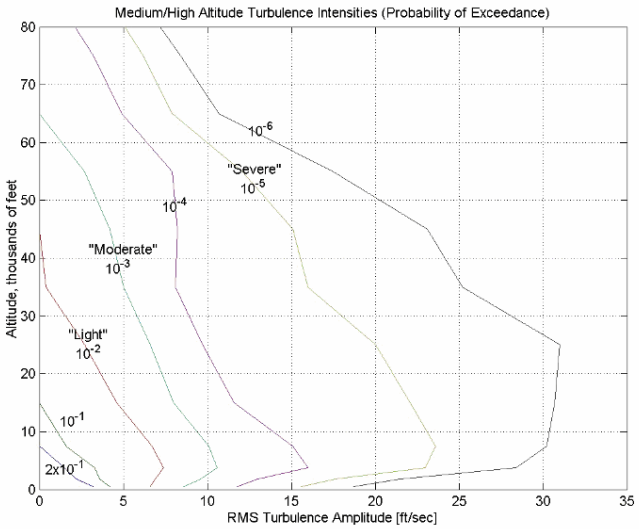

Figure 16: σ_w for different altitudes

4.2.3 Deterministic Simulation

Model verification involves examining the input-output relationship during different maneuvers, achieved from different input combinations. Three basic maneuvers - roll, pitch and yaw - are inherently coupled with aircraft translational and rotational motions, as seen in typical aircraft behavior, for example in the short-period mode. In the test cases examined, these maneuvers correspond to the following actuator combination inputs, each set denoted by Δ, as follows:

$$\Delta_{roll} = \{1, 1, 1, 1\}\delta, \tag{42a}$$

$$\Delta_{pitch} = \{-1, -1, , 1, 1\}\delta, \tag{42b}$$

$$\Delta_{yaw} = \{1, -1, -1, 1\}\delta. \tag{42c}$$

Where δ is a fin deflection angle, defined uniformly for all fins in the combination Δ, and its dynamics are given by (19). Each fin deflection angle is related to the state-space according to (11). Each simulation assessed the system response to the following input $u(t)$:

$$u(t) = \begin{cases} 1/60, & \text{if } t \leq 0.1, \\ 0, & \text{if } t > 0.1, \end{cases} \tag{43}$$

a 0.1-second pulse, with an amplitude of $u = 1/60$, for each input set Δ_i. The simulation demonstrates the coupling of aircraft motions and the amplification of elastic modal motions in the aircraft's response, while also enabling inspection of actuator dynamics and comparison of their time scale to the response time scales.

Figure 17 illustrates the control surface deflection response during a pitching maneuver. The fin's settling time is approximately 0.02 seconds, an order of magnitude faster than the system's fastest rigid body pole (≈ 0.14 seconds), as shown in the eigenvalue plot in Figure 7b. This implies that the fin response, especially the transient response, will not have a strong impact on the system dynamics. Furthermore, the second-order-like response suggests that the generated dynamics can be represented appropriately by a third-order model with one real and two complex poles.

In Figs. 18–20, both the rigid-body and elastic responses to different inputs are presented, illustrating the system's dynamic behavior. In all three cases, the dominant motion responses align with the intended maneuver, demonstrating the expected coupling between control inputs and aircraft motion. For example, in Fig. 18a, the primary motion observed is roll, consistent with the applied input, while secondary motions such as yaw and sideslip remain relatively small. Similarly, in Fig. 19, the pitch response is dominant, with minor contributions from

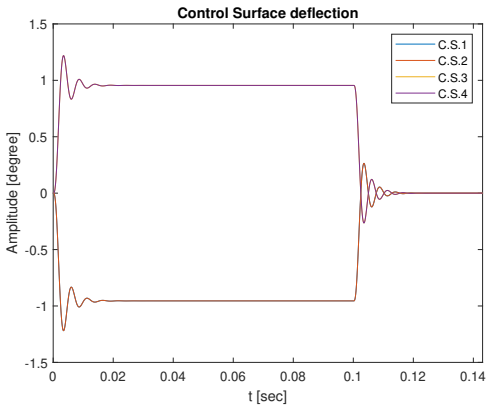

Figure 17: Fin deflection response

other degrees of freedom due to aerodynamic and structural coupling. These results highlight the fidelity of the simulation in capturing both rigid-body dynamics and elastic deformations.

Figure 18a shows the roll response, which exhibits first-order system behavior. This is confirmed by the stable real pole in Fig. 8, indicating a first-order system. Additionally, the time scale matches the expected settling time of a first-order system given by

$$T_{s_\epsilon} = -\frac{1}{p}\ln\left(\frac{1}{\epsilon}\right), \tag{44}$$

where p is the pole value (assuming a negative value for a stable converging response), and ϵ is the convergence percentage value. For $\epsilon = 2\%$, the settling time is

$$T_{s_{2\%}} = -\frac{3.91}{p} \approx 0.75[sec], \tag{45}$$

based on a pole value of $p \approx -7$, as in Fig. 8.

Pitch and yaw responses, shown in Figs. 19 and 20, are similar due to the model symmetry about the X-Y and X-Z planes. Consequently, the pitch and yaw inputs yield nearly identical responses, differing only by sign. The significant difference is in the elastic responses, which are in and out of phase due to the problem geometry (up-down vs. left-right motion). This symmetry of responses implies that it is sufficient to analyze only one of the two.

The short period response is seen in Fig. 19a with the coupled elastic response in Fig. 19b. As expected, the only significant displacement is in the Z direction. The short period poles in Fig. 8 are in $p_{sp} \approx -0.73 \pm j10.62$, its natural frequency of 10.6 $[rad/sec]$ and low damping value of $\zeta_{sp} = 0.0687$ are shown in the $\omega - V - g$ plot. The response is indeed only lightly damped and oscillates rapidly.

It is evident that the pitch input also excites a roll response, which can be explained by the system's coupling of motions in the two planes. Furthermore, the

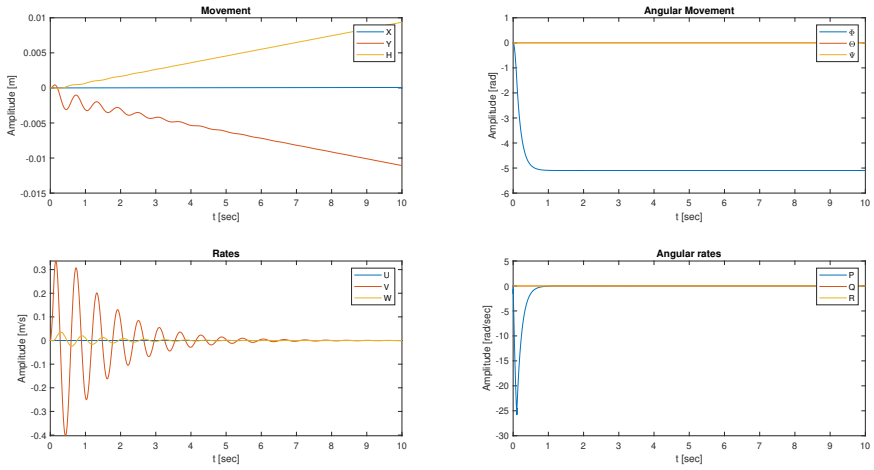

(a) Roll input - Rigid body response

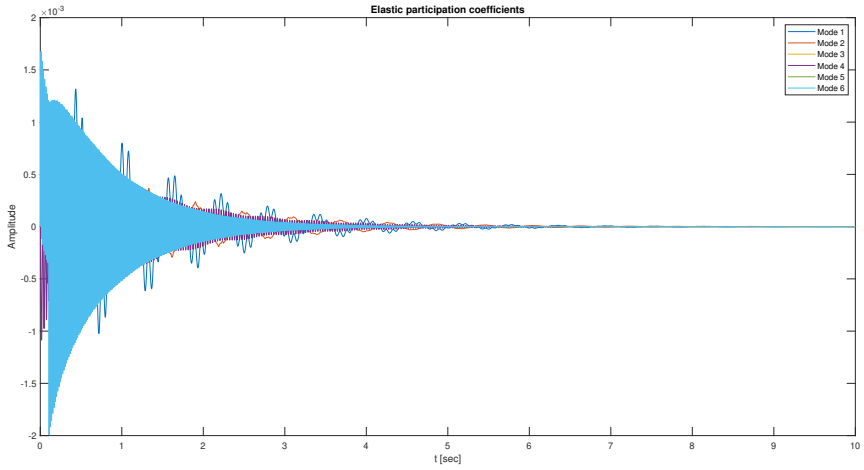

(b) Roll input - Elastic response

Figure 18: Roll input response

angular rate responses exhibit high-frequency content in addition to the dominant short-period frequency (which is now a rigid-elastic response). However, these higher frequency responses were of significantly smaller amplitude. The frequency contents of the signals are present in the response were identified using FFT over a simulation time of 100 [*sec*]. The results are presented in Figs. 21 and 22.

Figs. 21 and 22 show the frequency content of the system outputs for deterministic excitation. As expected, the peaks in the graphs correspond to the main aeroelastic frequencies of the system, aligning with the frequencies previously identified in the Bode plots, further verifying the accuracy of the simulation. Moreover, the dominance of the short-period mode and the first elastic mode is evident, as both exhibit higher amplitudes compared to the other modes. Nevertheless, all the system's modes are still present in the results, demonstrating that the simulation successfully captures the full dynamic behavior of the system, including both

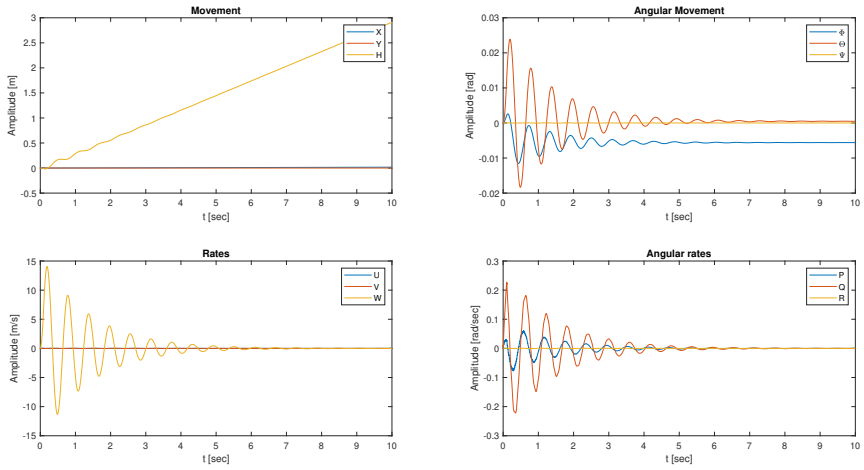

(a) Pitch input - Rigid body response

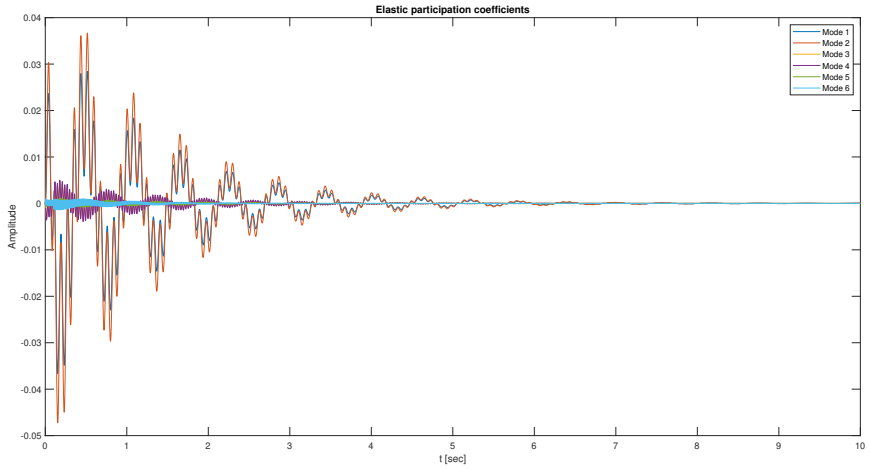

(b) Pitch input - Elastic response

Figure 19: Pitch input response

rigid-body and elastic contributions.

Analysis of the elastic modes confirms previous observations: pitch responses exhibit in-phase behavior for mode pairs 1-2, 3-4, and 5-6, while yaw responses show out-of-phase behavior. This is attributed to the geometry and the requirement for in- and out-of-phase control surface inputs (at 45°) to generate these motions. The dominant first mode is evident, confirmed by FFT analysis, with higher modes present at significantly lower, though non-negligible, amplitudes.

5 Future Work

Future research will continue to focus on simulating both strain and rigid body responses to control inputs, as well as estimating rigid body motions from strain

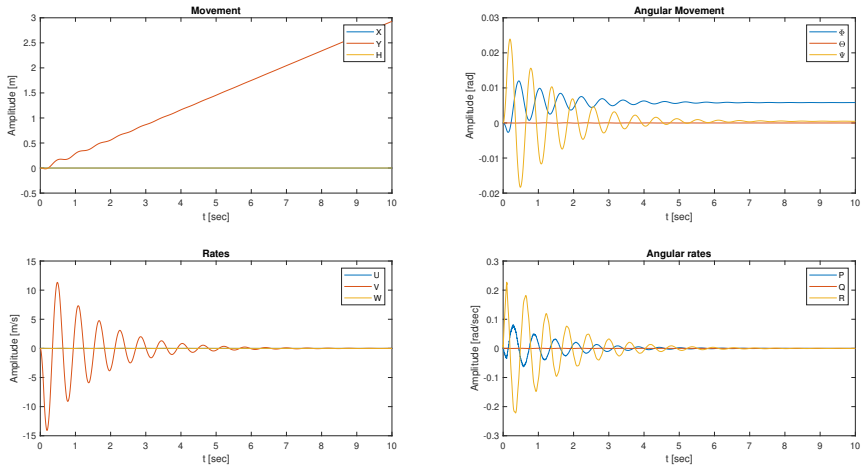

(a) Yaw input - Rigid body response

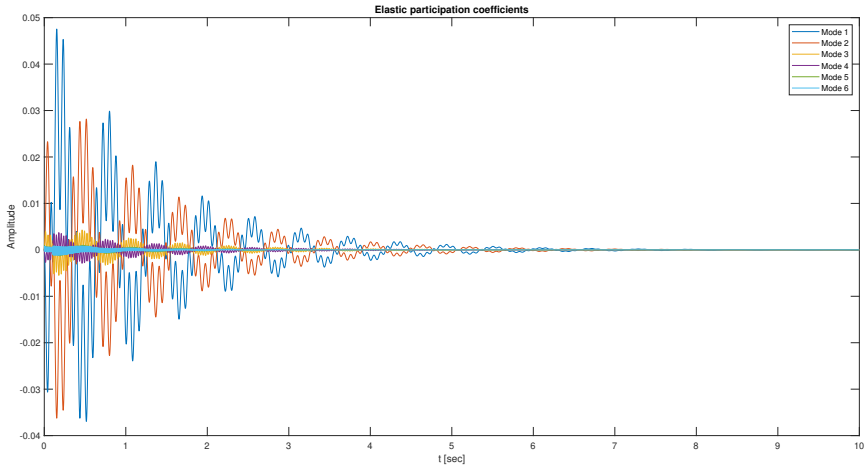

(b) Yaw input - Elastic response

Figure 20: Yaw input response

data using a Kalman state estimator. The simulation framework will be enhanced to fully incorporate the stochastic wind model and gravity effects. Additionally, a control algorithm will be developed, and the simulations will be expanded to cover a wider range of velocities and system parameters, enabling more comprehensive and robust analysis.

References

Baldelli, D. H., Chen, P. C., and Panza, J. (2006). Unified aeroelastic and flight dynamic formulation via rational function approximations. *Journal of Aircraft*, 43(3):763–772.

Bisplinghoff, R. L., Ashley, H., and Halfman, R. L. (2013). *Aeroelasticity*. Courier

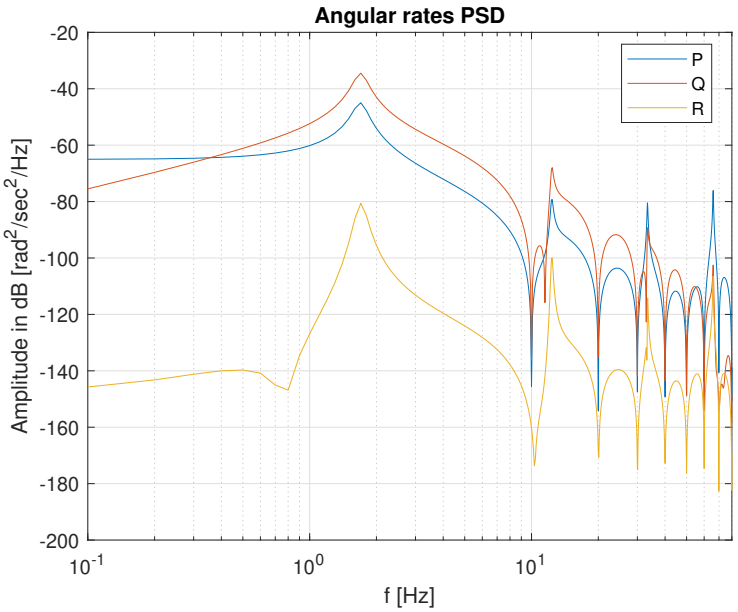

Figure 21: Angular rates frequency content

Corporation.

Genkin, I. and Raveh, D. E. (2024). Estimation of slender body elastic rates and accelerations using a combination of measured data. *International Forum on Aeroelasticity and Structural Dynamics*.

Karpel, M. (1980). *Design for active and passive flutter suppression and gust alleviation*. Stanford University.

MIL-F-8785C (1980). Flying qualities of piloted airplanes. Technical report, U.S. Department of Defense, Washington, D.C. U.S. Military Specification.

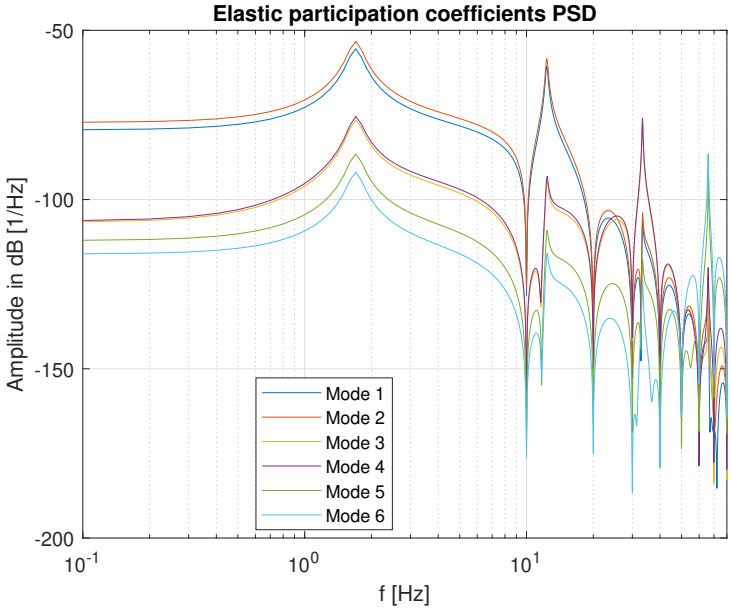

Figure 22: Elastic participation coefficients frequency content